Planetary and Space Science 182 (2020) 104758

Contents lists available at ScienceDirect

Planetary and Space Science

journal homepage: www.elsevier.com/locate/pss

Electrical properties of cometary dust particles derived from line shapes of TOF-SIMS spectra measured by the ROSETTA/COSIMA instrument

Klaus Hornung [a,*], Eva Maria Mellado [a], John Paquette [b], Nicolas Fray [c], Henning Fischer [b], Oliver Stenzel [b], Donia Baklouti [d], Sihane Merouane [b], Yves Langevin [d], Anais Bardyn [e], Cecile Engrand [f], Hervé Cottin [c], Laurent Thirkell [g], Christelle Briois [g], Paola Modica [g], Jouni Rynö [h], Johan Silen [h], Rita Schulz [i], Sandra Siljeström [j], Harry Lehto [k], Kurt Varmuza [l], Andreas Koch [m], Jochen Kissel [b], Martin Hilchenbach [b]

[a] *Universität der Bundeswehr München, LRT-7, 85577, Neubiberg, Germany*
[b] *Max-Planck-Institut für Sonnensystemforschung, Justus von Liebig Weg 3, 37077, Göttingen, Germany*
[c] *Laboratoire Interuniversitaire des Systèmes Atmosphériques (LISA), UMR CNRS, 7583, Université Paris-Est-Créteil, Université de Paris, Institut Pierre Simon Laplace (IPSL), Créteil, France*
[d] *Institut d'Astrophysique Spatiale, CNRS / Université Paris Sud, Bâtiment 121, 91405, Orsay, France*
[e] *DTM, Carnegie Institution of Washington, Washington, DC, USA*
[f] *Centre de Sciences Nucléaires et de Sciences de la Matière, Bat.104, 91405, Orsay Campus, France*
[g] *Laboratoire de Physique et Chimie de l'Environnement et de l'Espace(LPC2E), UMR CNRS 7328, Université d'Orléans, F-45071, Orléans, France*
[h] *Finnish Meteorological Institute, Climate Research, Erik Palmenin aukio 1, P.O.Box 503, FI-00101, Helsinki, Finland*
[i] *European Space Agency, Scientific Support Office, Keplerlaan 1, Postbus 299, 2200, AG Noordwijk, the Netherlands*
[j] *RISE Research Institutes of Sweden, Bioscience and Materials, Chemistry and Materials, Box 5607, 114 86 Stockholm, Sweden*
[k] *Tuorla Observatory, Department of Physics and Astronomy, University of Turku, Väisäläntie 20, 33 21500, Piikkiö, Finland*
[l] *Institute of Statistics and Mathematical Methods in Economics, Vienna University of Technology, Wiedner Hauptstrasse 7/105-6, 1040, Vienna, Austria*
[m] *Von Hoerner und Sulger GmbH, Schlossplatz 8, 68723, Schwetzingen, Germany*

A R T I C L E I N F O

Keywords:
Cometary dust
Rosetta mission
Electrical properties
Time-of-flight mass spectra
Sample charging

A B S T R A C T

Between Aug. 2014 and Sept. 2016, while ESA's cornerstone mission Rosetta was operating in the vicinity of the nucleus and in the coma of comet 67P/Churyumov-Gerasimenko, the COSIMA instrument collected a large number of dust particles with diameters up to a millimeter. Positive or negative ions were detected by a time-of-flight secondary ion mass spectrometer (TOF-SIMS) and the composition of selected particles was deduced. Many of the negative ion mass spectra show, besides mass peaks at the correct position, an additional, extended contribution at the lower mass side caused by partial charging of the dust. This effect, usually avoided in SIMS applications, can in our case be used to obtain information on the electrical properties of the collected cometary dust particles, such as the specific resistivity ($\rho_r > 1.2 \cdot 10^{10}\ \Omega m$) and the real part of the relative electrical permittivity ($\varepsilon_r < 1.2$). From these values a lower limit for the porosity is derived ($P > 0.8$).

1. Introduction

The COSIMA instrument (COmetary Secondary Ion Mass Analyser, Kissel et al., 2007) collected dust particles in the inner coma of comet 67P in an unprecedented state of preservation due to the impact at low speeds (a few m/s) onto highly porous and low reflectance metal targets (Schulz et al., 2015; Hilchenbach et al., 2016). During the 2 years of the comet escort phase, the instrument continuously measured and transmitted mass spectra from the collected dust particles, contributing to numerous aspects of their chemical composition. The elemental composition of the 67P particles is similar, within a factor of 3, to the one of CI chondrites for the inorganic fraction. As already measured in the particles of 1P/Halley, the 67P particles have a large enrichment in carbon compared to CI chondrites and the organic matter could represent about 45% of the mass of the cometary particles (Bardyn et al., 2017). The carbonaceous matter should be of high molecular weight (Fray et al., 2016) with a $N/C = 0.035 \pm 0.011$ (Fray et al., 2017) and $H/C = 1.04 \pm 0.16$ (Isnard et al., 2019). The cometary H/C elemental ratios are in most cases higher

* Corresponding author.
E-mail address: klaus.hornung@unibw.de (K. Hornung).

https://doi.org/10.1016/j.pss.2019.104758
Received 17 April 2019; Accepted 24 September 2019
Available online 28 September 2019

than the values found in the Insoluble Organic Matter (IOMs), extracted from carbonaceous chondrites. This could imply that cometary organic matter is less altered than the organic matter in chondritic IOMs. Evidence for calcium-aluminium-rich inclusions (CAIs) has been found in one of the dust particles (Paquette et al., 2016). The isotopic ratios $^{34}S/^{32}S$ and $^{18}O/^{16}O$ are both consistent with the terrestrial standards within the error bars, but the sulfur ratio is significantly higher than that measured in several gaseous species in the coma of 67P (Paquette et al., 2017, 2018).

In addition to chemical information, COSIMA delivered images of the collected dust from the built-in microscope camera COSISCOPE which enabled analysis of the dust flux and its time evolution along the comet's trajectory inbound and outbound from the sun (Merouane et al., 2016, 2017). The images further revealed that the collected dust particles are agglomerates made up of smaller subunits (Langevin et al., 2016). An analysis of the fragmentation caused by the impact at collection led to the conclusion that, in many cases, those subunits possess a mechanical stability of their own and therefore have been denoted as „elements" (Hornung et al., 2016). Atomic force microscope analysis from the MIDAS instrument onboard Rosetta (Bentley et al., 2016; Mannel et al., 2016) suggested that these elements have further substructures on the submicron scale. Optical scattering studies revealed volume scattering on the scale of the elements and that the dust has high transparency and likely high porosity (Langevin et al., 2017).

The collected dust particles turned out to have low electrical conductivity such that those elements of the agglomerate, which are located within the footprint of the spectrometer's primary ion beam ($8kV\ In^+$), can be positively charged. Small displacements of the elements were often detected in the images taken immediately after the spectra acquisition. The charging could even lead to fragmentation of larger particles which survived the impact at collection undamaged, as has been shown by dedicated *in situ* experiments (Hilchenbach et al., 2017). The fragment size distribution due to the Lorentz forces, induced by charging, was almost identical to the case of impact fragmentation, i.e. two completely different physical fragmentation mechanisms result in a similar outcome and the conclusion is that the elements are already present in the incoming dust as separate entities. When the COSIMA operations began to focus on negative mode mass spectra, an asymmetry in the line shapes was observed, consisting in a large contribution preceding the main mass peak, expanding up to 10 times the width of the main peak, which was still narrow and located at the expected mass position. This asymmetry appears because the electrical potentials of COSIMA's time-of-flight section are distorted from their optimum values, due to the charging of the dust particles, and we found that it reflects information on the electrical properties of the dust. This information would have been lost by the use of an electron gun to compensate the charging, which is usually the case in secondary ion mass spectrometry operation in the laboratory. Such electrical properties, especially the real part of the permittivity, can be used to derive limits on the dust's porosity. This method represents a standard tool in geology (e.g. Rust et al., 1999) and it is also used when probing the surface and subsurface areas of airless bodies in the planetary system, mostly by remote radar techniques (e.g. Campbell and Ulrichs, 1969; Boivin et al., 2018; Hickson et al., 2018). During Rosetta's lander Philae operation in November 2014, the radiowave transmission instrument CONSERT and the impedance probe SESAME-PP derived the porosity of the comet's subsurface from electrical permittivity data, the former by radio waves crossing the comet nucleus, and the latter injecting an AC current in the low frequency range at the landing near-surface (Kofman et al., 2015; Hérique et al., 2017; Lethuillier et al., 2016).

The present report analyzes the line asymmetry observed in COSIMA's negative secondary ion mass spectra with the goal to derive electrical properties, and from this an estimate of the porosity of the dust's elements. Sec. 2 briefly introduces the reader to the problem by giving details of the physical environment on the collection targets on which the dust is trapped, showing examples of the asymmetrical line shapes and reporting on tests with COSIMA's laboratory model ("reference model, RM"). Sec. 3 presents a numerical scheme to calculate the line profiles by modelling the relevant line broadening mechanisms with open parameters, to be fitted to COSIMA's flight spectra. Since it has been observed that the charging reaches a limiting value after less than a second, a current must flow in the stationary state from the charged elements to the grounded target. In Sec. 4 this treatment is applied to the COSIMA negative mode mass spectra and values for the model parameters are derived, the charging potential being the most important one. Further technical details are provided in the Appendix. The implications for the comet's dust electrical properties are then discussed in Sec. 5. Based on the findings on the charging potential and the kind of current conduction, a lower limit for the specific resistivity of the elements is derived. Using a series of spectra acquisitions with increasing exposure time gives an upper limit for the charge-up time. By combining with the lower limit of the resistivity, an upper limit for the real part of the relative electrical permittivity at direct-current conditions (DC) follows. This upper limit is then used to derive a lower limit for the porosity of the dust's elements by applying known mixing rules, which determine the permittivity of the porous matter from the corresponding values of the compact constituents.

2. Observational data

2.1. Physical environment of the collected dust on the target

Dust particles from comet 67P were collected by impact onto $1 \times 1\ cm^2$ sized metal targets (Au or Ag) covered with a 10 to 20 μm thick layer of a highly porous metal structure having grain sizes of a few tens of nanometers. This layer is referred to as "metal black" due to its deep black appearance in visible light which provides an ideal background for optical inspection. The speed of the incoming dust particles was a few m/s (Rotundi et al., 2015). Fig. 1 shows a SEM image of a metal black structure with collected particles embedded in it from pre-flight laboratory collection experiments (Hornung et al., 2014). The image illustrates what was expected prior to the cometary encounter: many dust particles of micron size dispersed amid the metal black within the ion beam's footprint area (about $35 \times 50\ \mu m^2$) such that the conductive target can compensate possible charging of the dust particles.

The reality at the comet turned out to be different. Fig. 2 shows a COSISCOPE image of 67P dust particles collected on a gold black target at a resolution of about 10 μm (by using the resolution enhanced Nyquist mode, see Langevin et al., 2016), much lower than in the laboratory SEM image of Fig. 1. The dust particles are larger than expected, a few 100 μm up to 1 mm, as seen by their lateral extent as well as their cast shadow. The image clearly shows the agglomerate structure with subunits ("elements") having sizes of several tens of micrometers such that a few of

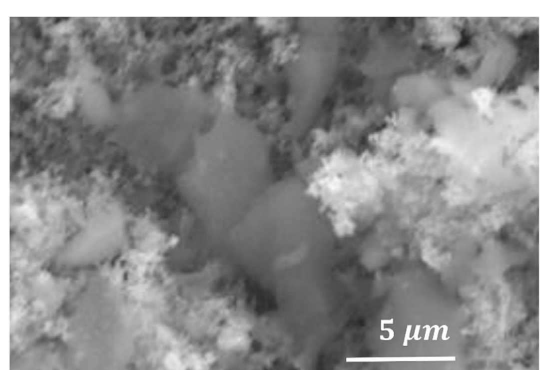

Fig. 1. Pre-flight laboratory collection experiments: SEM image showing dust particles (dark smooth areas) embedded in highly porous silver black (the fluffy and lighter material on the image).

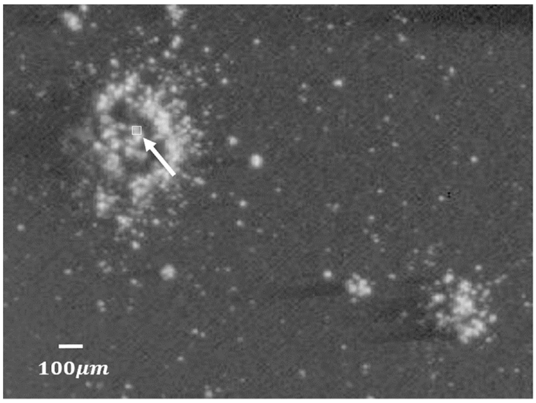

Fig. 2. Dust particle Jessica (upper left), collected on the gold black target 2CF on Jan. 26, 2015, imaged Feb. 10, 2015 (white square: position of SIMS measurement). For naming conventions see Langevin et al., (2016).

them may be located within the footprint of the primary ion beam.

2.2. Observation of asymmetrical line shapes in the COSIMA negative spectra

During the SIMS analysis of the collected dust particles, the spectra in negative ion mode featured mass lines with shapes changing in a very peculiar way: Left from the line peak, i.e. at lower mass values, there evolves a long signal extension which grows in intensity when the dust particle gets increasingly into the focus of the ion beam. Generally asymmetries appear whenever there is a deviation of the spectrometer's electrical potential settings from their optimum design values. However, operational variations of the instrument settings could be ruled out, since they were continuously measured and transmitted to ground together with every spectrum and did not show any changes. It thus became obvious that surface charging was building up on the dust particle, a known side effect in laboratory SIMS applications when the probe has low electrical conductivity (Werner and Morgan, 1976).

Fig. 3 shows examples for the mass lines ^{12}C, ^{16}O, ^{32}S and ^{197}Au measured at the dust particle of Fig. 2. Due to their special shape we denote these profiles hereinafter as "left shoulder" profiles. While most of the line profiles show this asymmetry, some do not, such as ^{197}Au, which obviously originates from uncharged target areas which may remain within the focus of the primary ion beam. In contrast, when the primary ion beam hits the gold black target only, all lines show symmetric shapes. Due to the SIMS high detection sensitivity, even on these "empty" parts of the gold black target one observes, besides gold, a multitude of lines from surface contaminants, e.g. C, O and S.

2.3. Laboratory tests of charging with the COSIMA reference model

When the dust particle gets a positive bias with respect to the target due to charging, then negative secondary ions do not experience the full extraction voltage U_{EL} of the instrument (see Appendix), but a value reduced by the bias. In order to quantify the response of COSIMA to such a change, a series of mass spectra has been measured with the laboratory instrument of COSIMA ("reference model RM"). A target (a carbon strip from a commercial resistor) was set to various constant positive potentials. Fig. 4 shows the results for the example of the negative oxygen line. Depending on the value of the positive target potential, the $^{16}O^-$ line shifts as a whole towards earlier times (to lower mass). This shift means that negative ions desorbed from positively biased targets arrive earlier at the detector, despite being slower as a result of the reduced extraction voltage. This "reverse" behaviour is due to the special two-stage reflectron used (Mamyrin, 2001). Fig. A1 of the Appendix shows the corresponding setup. Ions with lower kinetic energy dive less deeply into the space between grids 4 and 5 than their companions with higher speed and they leave this space earlier. In their further travel the faster ones cannot catch up and finally the slower ones arrive earlier at the detector. The Mamyrin version has the advantage of being "energy-focussing" when operating at its optimum voltage configuration, i.e. it efficiently corrects the spread in the initial energy of the secondary ions at emission

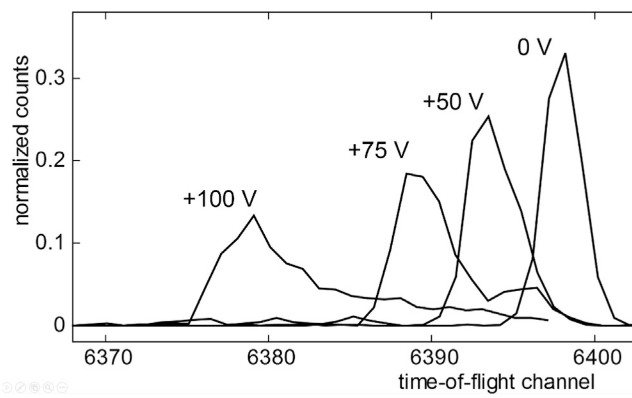

Fig. 4. Negative ion mode mass spectra obtained with the COSIMA-RM laboratory model showing the left shift and the deformation of the $^{16}O^-$ line when the target is positively biased (time channel bin size = 1.956 *nsec*).

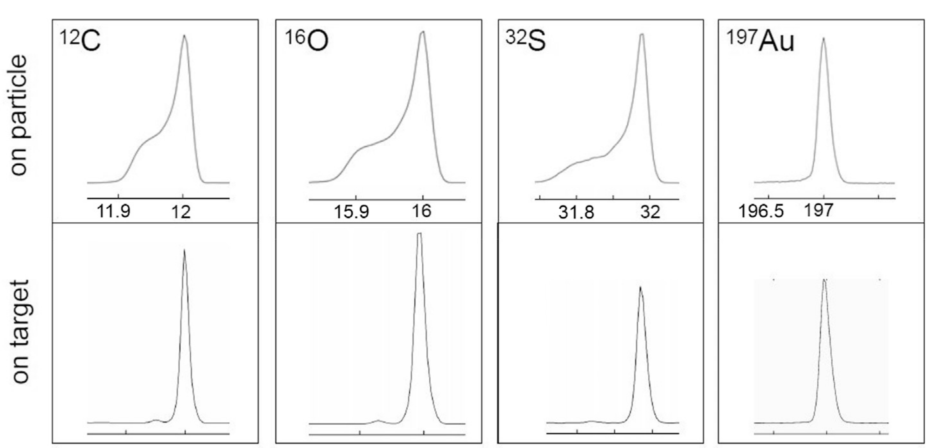

Fig. 3. Upper panels: Asymmetrical TOF-SIMS line shapes in the negative ion mode mass spectra from particle Jessica on the gold black target 2CF, sum of 1001 spectra. Lower panels: Corresponding lines when the primary ion beam hits an empty gold black target position, located far from Jessica (about 4000 μm), sum of 69 spectra. Linear vertical axis, arbitrary units.

(a few eV), achieving spectral lines with high mass resolution. However, it reacts very sensitively and loses this capability when the extraction voltage deviates from its optimum due to charging. As consequence, the profiles in Fig. 4 feature a large tail to the right, which becomes broader with increasing charging potential (the tails shown in Fig. 4 are consistent with a Maxwellian distribution having a characteristic energy of $U_0 = 5 - 10\ eV$).

The RM tests clarified COSIMA's reaction to a uniform charging level imposed by a fixed bias at a conductive target. However, in the case of COSIMA's flight data, where the charging is produced by the primary ion beam, there is a continuum of charging potentials from zero up to a maximum value, caused by the spatial Gaussian profile of the primary ion beam. Therefore, one does not observe a shift of the whole line, but a broad continuum to the left, which represents a superposition of left-shifted profiles of the kind shown in Fig. 4. It is interesting to note that Fig. 4 already gives a first estimate of the maximum shift of about 20 time bins for a charging of 100 V for the case of oxygen ions, in agreement with the extent of the "left shoulder" one observes in COSIMA's flight spectra.

3. Modelling line shapes in the presence of charging

The empirical insights into the problem, as discussed up to now, allow us to establish a model to calculate the line shape. It is built upon several open parameters, which are then fitted to the COSIMA negative spectra. Within this model, the spectral amplitude $A(t)$ follows from a superposition of three major broadening contributions:

$$A(t) = \int \delta(t - t_{det}(t_0, v_0, r)) \cdot f_t(t_0) \cdot f_v(v_0) \cdot f_r(r)\ dt_0 dv_0 dr \tag{1}$$

δ is the delta function and t_{det} is the arrival time at the detector. The equation links the spectral amplitude $A(t)$, or in other words, the probability of a secondary ion to arrive at a time t at the detector, to the following variables: 1. The moment of generation at the target t_0, its abundance $f_t(t_0)$ being represented by a Gaussian, which describes the time dependence of the primary ion pulse, 2. the initial emission velocity of the secondary ions (axial component), v_0, its abundance $f_v(v_0)$ being represented by a Maxwellian, 3. the radius r within the primary beam relative to the beam center (in the plane normal to the beam axis) from which the primary ion beam current density (ions per unit area and unit time), $i(r)$, depends via a Gaussian. The probability for a certain radius is then $f_r(r) = 2\pi r \cdot i(r) \cdot f_{tr}(U_c)$, where $f_{tr}(U_c)$ accounts for the transmission loss due to the charging potential $U_c(r)$ (see Appendix). $U_c(r)$ itself can be expressed as a function of $i(r)$ as will be discussed below. All three variables, (t_0, v_0, r) contribute to the broadening of the line and our finding is that they are sufficient to represent the most important features of the measured line shapes. The detector arrival time t_{det} is the sum of the generation time t_0 and the passage time t_{TOF} of the secondary ions through the time-of-flight section of the spectrometer: $t_{det}(t_0, v_0, r) = t_0 + t_{TOF}(v_0, r)$, and the way t_{TOF} is calculated is explained in the Appendix. The numerical solution of Eq. (1) uses discretized values of t_0, v_0 and r. The integration is performed using the same binning technique as the COSIMA electronics: a certain ion generated at time t_0, having an initial velocity of v_0 and starting from a location which is charged by some amount $U_c(r)$ is sent through the instrument and its arrival time t_{det} is sorted into an array of equally spaced bins for the variable t (bin size = 1 TOF unit). By sending a large number of ions (several 10^6) through the instrument, and adding up the counts that fall into each time bin, a discrete data set for the spectral amplitude $A(t)$ is generated.

The dust charging potential depends on the primary ion beam current and the dust's electrical properties (Werner and Morgan, 1976). Suppose that the primary beam (8 keV positive ions of isotopically clean ^{115}In) hits a dust layer of height h of the agglomerate dust structure as shown schematically in Fig. 5. A certain surface area receives a current I and develops a potential difference $U(t)$ between top and bottom depending

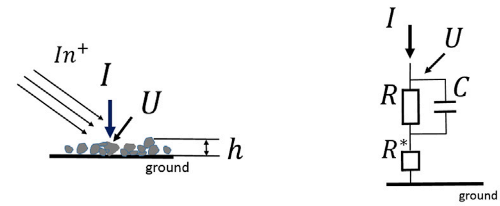

$$(\, U(t) = I \cdot R^* + I \cdot R \cdot \left(1 - e^{-t/\tau}\right);\ t \gg \tau:\ U(t) \to U_c = I \cdot (R + R^*);\ \tau = R \cdot C)$$

Fig. 5. Equivalent scheme for the buildup of the charging potential U.

on the resistance R and capacity C of individual elements of the agglomerate (R^* accounts for a possible contact resistance between the bottom of the dust and the grounded target). The primary ion beam is pulsed with a repetition rate of 1.5 kHz, the pulse width Δt_p being a few ns, yet it acts as a DC current because the rise time τ of charging has been found to be on the order of a second. After this initial rise time the charging potential keeps a constant value U_c, which leads to the conclusion that a steady current must flow through the dust to the target during the spectra acquisition time of a few minutes. Although extremely small (in the order of 1/10 of a pA), this current is essential to maintain the charging of the dust. Thus the cometary dust particles are not insulators, but poor conductors and the electrical behaviour cannot be described by electrostatics alone. The initial rise time τ has no influence on the interpretation of the spectral line shapes and the measured values of the charging potential, U_c, always represent the asymptotic steady state limits. However, the rise time becomes important when discussing the dust permittivity in Section 5.

The dependence of the steady state limit of the charging potential on the current density, which is caused by the primary ion beam, has to be determined from the shape of the spectral lines. At this point it should be noted, that the line shape does not depend on the absolute value of $i(r)$, but only on its radial distribution. However, the absolute value will come into play when discussing electrical properties below. With the maximum charging $U_{c,max}$ and the maximum current density i_{max} occurring at the center of the primary beam's footprint, the potential-current relationship can be formally written in a dimensionless form:

$$\frac{U_c(r)}{U_{c,max}} = \phi(y);\ y = i(r)/i_{max} \tag{2}$$

Several functions for the dependence of the reduced charging potential $\phi(y)$ on the reduced current density y have been tested resulting in the following empirical dependence with an open shape parameter ξ:

$$\phi_\xi(y) = \frac{\arctan\left(y/\xi\right)}{\arctan\left(1/\xi\right)} \tag{3}$$

The physical significance of ξ becomes clear, when considering its limits as illustrated in Fig. 6. For small values of ξ, already small currents cause a final saturation charging level $U_{c,max}$. In this case, the width of the distribution of U_c values would be narrow. In the limit of $\xi \to 0$ there is only one value for U_c (a spatially uniform charging caused by sideward charge transport) and consequently the spectral line is shifted to the left as a whole. In the limit of large ξ, potential and current are proportional ($\phi(y) = y$), which means "ohmic" behaviour is present. The ansatz of Eq. (3) gives a possibility to formally include all possible situations between uniform charging and "ohmic" behaviour and then derive from the spectra which case prevails.

The contribution to the line profile from the charged areas can be interpreted as a weighted superposition of profiles shifted in time by an amount corresponding to the value of the charging potential U_c, where f_r is the weight function. Fig. 7 shows an example for f_r in the case of "Ohm's limit": $\phi(y) = y$. The sharp decrease close to $\phi = 1$ is responsible

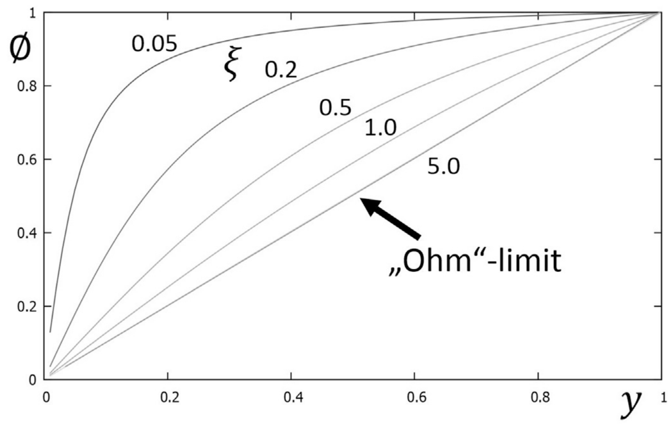

Fig. 6. Dependence of the reduced charging potential $\phi(y)$ on the reduced current density y.

for a characteristic cutoff of the line profile at its left end, as observed in the COSIMA flight spectra. COSIMA data analysis showed that there are cases when the primary ion beam does not only hit the dust particle, but partly also the target where no charging appears. Therefore an additional parameter is introduced, w_1, describing the fraction of ions in the spectrum originating from uncharged areas (from charged is then: $w_2 = 1 - w_1$). In addition, along with the negative ions, there is a small contribution to the spectral line coming from secondary electrons generated by ion impact onto a grid, located immediately before the detector (see Appendix, Fig. A1, grid No. 8). These electrons produce a lower mass spectral feature, left from the ion contribution. Their fraction w_{el} is a few percent of the total line integral as suggested by spectra on no-dust (target) positions (e.g. the lower panels, "on target" of Fig. 3). The final line profile is obtained by adding up the contributions from uncharged and charged areas as well as secondary electrons, each calculated separately with the above described binning technique, and weighting them with w_1, w_2 and w_{el} respectively. Both, the amplitudes of the model profile and the COSIMA spectral data, are then normalized to 1. This ensures that the line integrals of model and data are identical, giving freedom only for the shape of the profile. The model time t is finally converted into a mass value m via: $m = \left(t/a\right)^2$, where a is a parameter (sometimes called the "stretch parameter"), which depends on the instrument's electrical potential settings. It is adjusted using the measured spectra. It turned out that all calculated times fall into a time-interval from about $13 \cdot \sqrt{M}$ time bins left from the line center to about $5 \cdot \sqrt{M}$ time bins right, which defines the time window for the fit, the time bin unit being 1.956 *nsec* and M being the nominal mass number of the spectral line under consideration, for example $M = 15.9955$ for the oxygen isotope $^{16}O^-$.

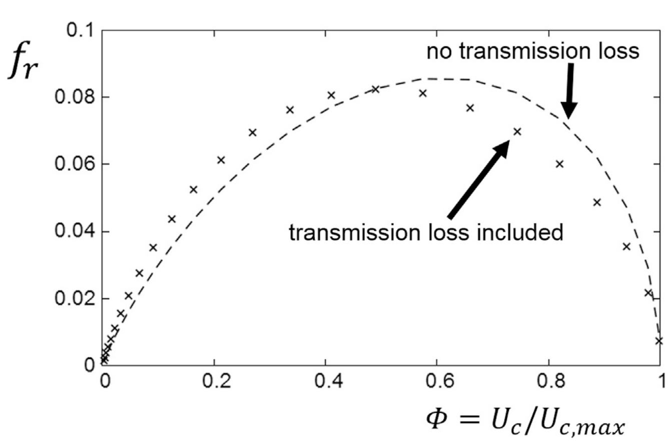

Fig. 7. Probabilities for individual charging potential values for the case of $\phi(y) = y$. The example uses 25 values for the discretization and the transmission loss is for the example of $U_{c,max} = 100\ V$.

Table 1
Summary of parameters.

ξ	shape parameter of the charge function Eq. (3).
$U_{c,max}$	maximum charging at the footprint of the primary ion beam center (*Volt*).
U_{01}	Maxwell energy parameter uncharged areas (eV).
U_{02}	Maxwell energy parameter charged areas (eV).
Δt_p	pulse width (full width at half maximum) of the primary ion beam (*nsec*).
w_{el}	fraction of secondary electrons from grid 8 (see Appendix).
w_1	fraction of ions from uncharged areas (charged areas: $w_2 = 1 - w_1$).
a	stretch parameter (in units of $1.956 ns/\sqrt{M}$).

The spectral data are used in a rebinned version and the comparison between calculated and measured line profiles is done on the mass scale. The rebinning process accounts for small variations in the instrument status over time (e.g. potential values) which lead to small variations in the position in time of the main known mass lines. The first step of the rebinning process is a dead time correction of the spectra, followed by calibration and a final interpolation of the data into a fixed time/mass scale. Only after such a procedure can many spectra be properly added to improve statistics without introducing artificial broadening. However, by this procedure the connection to the original time base of the instrument is lost, which means that now the experimental input is always amplitude versus mass. The adjustable parameter a then makes the connection between mass and the model time.

The evaluation of the 8 parameters (summarized in Table 1) is facilitated by the fact that each of them has its largest influence only in certain parts of the profile. For example, the time width of the primary beam pulse, Δt_p, is important close to the line maximum, but does not influence the shoulder close to its left boundary whereas the maximum charging $U_{c,max}$ is important at the left boundary, but not close to the line maximum. Our observation is that the parameters generally do not show big variations, such that a good initial guess can be defined and the number of iterations is small (typically 3 to 5). Some of the parameters can be easily estimated. For instance, Δt_p can be inferred from ions originating from the target (typically $5 - 10$ *nsec*). The secondary electron fraction, w_{el}, cannot exceed a few percent, since the grids of the instrument have a transparency higher than 90%. Initial energies of secondary ions are known to be on the order of several eV, extending up to $5 - 25\ eV$. In the end, only three parameters with a large influence remain: The shape parameter ξ, the maximum charging potential $U_{c,max}$ and the fraction of ions from uncharged areas, w_1 (charged: $w_2 = 1 - w_1$). Therefore optimization begins with these and then a fine-tuning of the others leads to a rapid convergence.

4. COSIMA negative mode spectra

The first example contains a very long measurement ($\approx 48\ h$) on the dust particle Jessica on target 2CF. A sum spectrum is used, consisting of a total of 1001 negative spectra acquired at 4 positions which are 30 μm apart from each other (marked as the corners of a white square in Fig. 2). Jessica data show the most pronounced left shoulder of all measured particles. Fig. 8 shows the individual data points (+) of the sum spectrum together with the model values (solid line) for the oxygen line. To be correct, both curves of Fig. 8 are histograms, but plotted as points and line for the sake of a clearer perception of the very small differences between data and model. The fit result shows that the shape parameter ξ is equal to 1, which is close to Ohm's limit. Fig. 9 shows an example of a very wide left shoulder from particle Jakub corresponding to high charging potential. Since in this case the data are averaged over only a few individual spectra, fluctuations are present originating most likely from spatial variations in the dust coverage within the primary ion beam's footprint. Most of the ions originate from the charged dust particle in this example, i.e. a low value of w_1. Fig. 10, particle Juliette, shows an example of an exceptionally narrow left shoulder

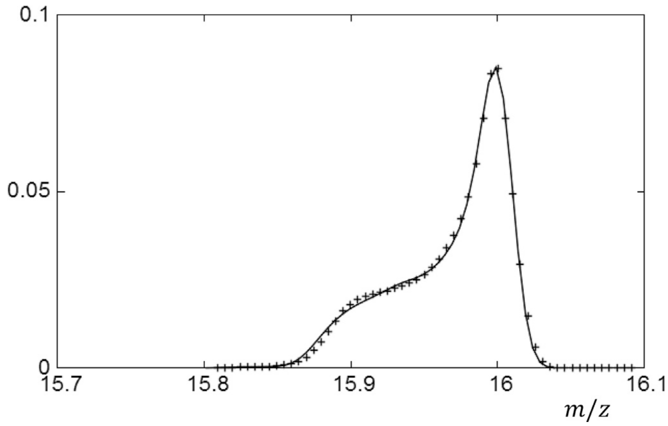

Fig. 8. Oxygen line profile: Normalized spectral amplitude (counts/total counts contributing to the oxygen mass line) versus m/z. Particle 2CF Jessica: + = spectral data, sum of 1001 spectra. Solid line: present model, Eq. (1). Parameters: $\xi = 1, U_{c,max} = 98\ V, U_{01} = 10\ eV, U_{02} = 4\ eV, \Delta t_p = 9\ nsec, = 0.02,\ w_1 = 0.23,\ M = 15.9955,\ a = 1601.3$.

corresponding to a maximum charging potential $U_{c,max}$ of only 67 V and it has a low charged fraction (high value of w_1).

To demonstrate how sensitive the results are to changes in the individual parameters, Fig. 11 contains parameter variations for the example of Fig. 8. It shows that the maximum charging potential $U_{c.max}$ determines the left cutoff of the shoulder and the dependence is very sensitive, i.e. a few Volts difference yields in a significant difference. Large variations in the shape parameter ξ would deform the profile in a way which is not observed in the data. Variations of a few *eVs* in the emission energy U_{02} of the charged areas causes a characteristic change in the line shape. Variations in the uncharged fraction parameter w_1 do not influence the shape of the left shoulder, but its vertical level. Although the contribution to the spectral signal resulting from the secondary electrons is only a few percent, it is in some cases significant to recognize the left end of the shoulder. Fig. 12 shows variations of w_{el} for the example of 1D2 Juliette in logarithmic scale to better recognize details of the left end of the profile. The main cutoff is connected to the maximum charging and the electron signal occurs before it, since the electrons (in Fig. 12 denoted by "e^- precursor") arrive earlier at the detector plate than the ions which caused them. The figure also shows that the model of Eq. (1) represents the data over 3 orders of magnitude down to the noise level.

More example particles have been investigated with the present procedure. Table 2 contains their reference data and the results of the corresponding fits are summarized in Table 3. In all cases high values for

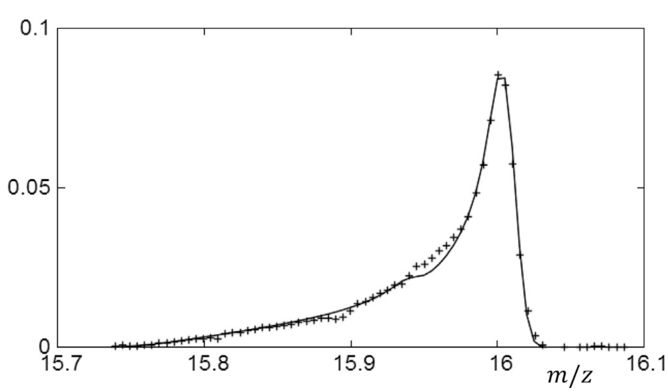

Fig. 9. Oxygen line profile, example: high charging potential: Particle 2D1 Jakub: + = spectral data, sum of 10 spectra. Parameters: $\xi = 5, U_{c,max} = 129\ V, U_{01} = 10\ eV, U_{02} = 10\ eV, \Delta t_p = 6\ nsec, w_{el} = 0.04, w_1 = 0.03,\ M = 15.9955,\ a = 1601.0$.

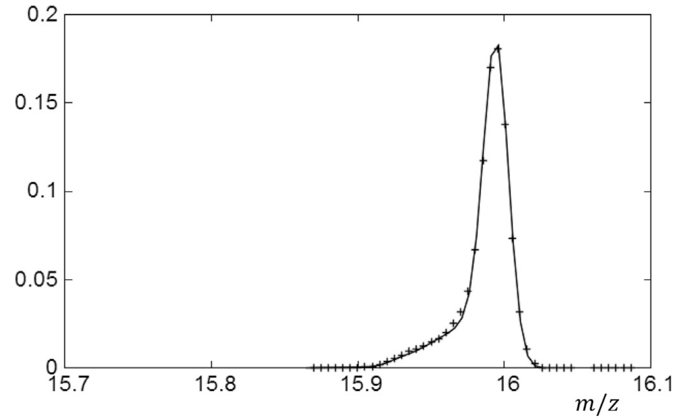

Fig. 10. Oxygen line profile, example: low charging potential and low charged fraction: Particle 1D2 Juliette: + = spectral data, sum of 12 spectra. Parameters: $\xi = 2, U_{c,max} = 67\ V, U_{01} = 10\ eV, U_{02} = 5\ eV, \Delta t_p = 7.5\ nsec, w_{el} = 0.02, w_1 = 0.70, M = 15.9955, a = 1601.7$.

the shape parameter were found: $1 \leq \xi \leq 5$. This means that the charge transport is close to the case of an Ohmic resistor. The initial kinetic energy of the ions U_{01} originating from non-charged areas has little influence on the left shoulder structure, whereas the initial kinetic energy of the ions from the charged areas, U_{02}, enters significantly. Here, one has to recall that the model introduced Maxwellian distributions of the axial component of the emission velocity because the exact angular emission characteristics of the secondary ions is hard to define for a surface of high and unknown roughness. Low values (particles Jessica and Juliette) may correspond to more diffuse emission leading to small contributions in axial direction. The division into charged and uncharged fractions, characterized by w_1, shows large variation, between 0 and 70%. This is especially an issue when using the present scheme for later interpretations of negative spectra. The fit parameters of Table 3 are for the ^{16}O peak. For the particles Juliette, Gunter and Jakub, the corresponding parameters for ^{32}S are added to give an idea about mass number dependences. In the case of Juliette, sulfur seems to originate in less proportion from target areas compared to oxygen as can be seen from the lower value of the uncharged fraction w_1. Emission energies U_{02} from charged dust areas might be dependent on the ion species (e.g. Juliette and Gunter). The table contains, in addition to the fit parameters, the values for the mean height h of the particle layer at measurement position as estimated from the cast shadow at images taken after the SIMS analysis. They show an increase of the charging potential with height.

The present model considers a homogeneous target for which the probabilities of individual potentials $U_c(r)$ only depend on the spatially varying current density $i(r)$ of the primary beam. This is the reason why averaged spectra are used since spatial variations in the dust properties and morphology are damped when the primary beam slightly shifts during the SIMS scan of the dust particle. As mentioned above, particle Jakub (Fig. 9) is an example for such variations when only few spectra

Table 2
Reference data for the spectra used (sum of N individual spectra, each with an acquisition time of 2.5 min; for naming conventions see Langevin et al., 2016).

Particle name	Collection start date	N	SIMS analysis date
2CF Jessica Lummene.2	2015/01/26	1001	2016/04/01–2016/04/04
1CD Barmal Orivesi.4	2015/07/31	8	2015/08/13
1D2 Juliette Hankavesi.1	2015/10/23	12	2015/11/18
1D2 Gunter Jerisjarvi.1	2016/02/29	96	2016/04/14
2D1 Jakub Toivesi.2	2015/05/11	10	2015/06/12
2D1 David Toivesi.2	2015/05/11	6	2015/06/12
2D1 Sora Ukonvesi.4	2015/05/22	12	2015/06/17

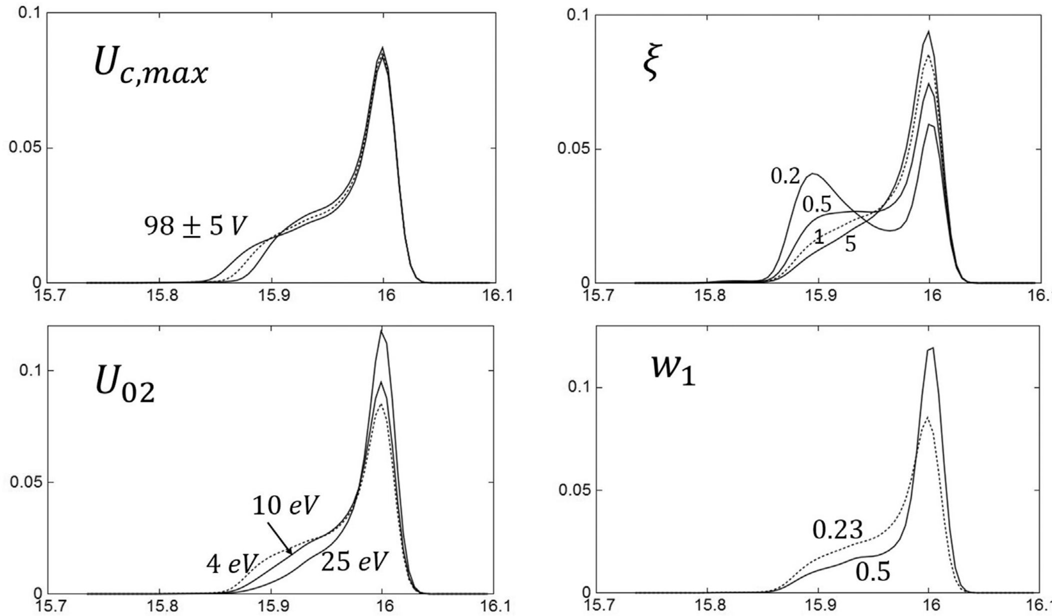

Fig. 11. Parameter variations around the profile of 2CF Jessica (dotted line: fit of Fig. 8).

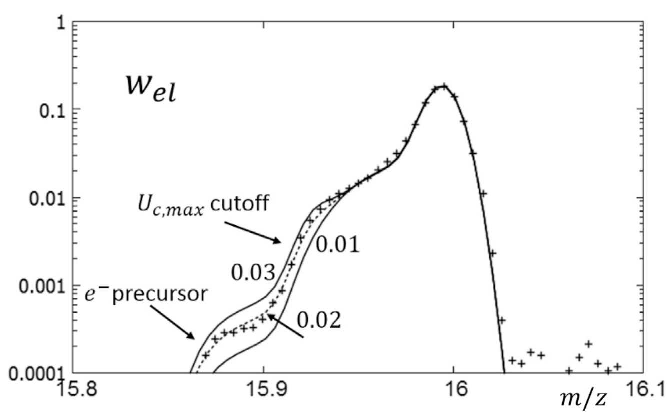

Fig. 12. Variation of the electron contribution w_{el} for the example of 1D2 Juliette (+= spectral data, dotted line: best fit; $w_{el} = 0.02$).

have been added. This structural effect becomes even more apparent for single spectra. We expect information on the morphological structure hidden in these spectra.

5. Information on electrical properties of the collected cometary dust

We have found that the cometary dust material when subject to a current, caused by the primary ion beam, acts like an ohmic resistor since the potential U_c is approximately proportional to the local current density i . The very close agreement between the line shape fits and COSIMA's flight spectra assures the reliability of the method and that it represents a direct way to measure this potential. The maximum charging potential $U_{c,max}$ varies with the height h of the dust layer, an information that can be used to derive the specific resistivity. Fig. 13 shows that the values of Table 3 follow a linear dependence with an offset U_{off} of about 45 V, likely being due to an interface contact resistance between dust material and metal black. Then the specific resistivity ρ_r can be expressed as:

$$\rho_r = \frac{U_{c,max} - U_{off}}{h} \cdot \frac{A_f}{I_{tot}} = b \cdot \left(\frac{A_f}{I_{tot}}\right) \tag{4}$$

where A_f is the footprint area of the primary ion beam and I_{tot} is the total current, induced by the primary ion beam. The specific resistivity ρ_r can be derived either from the slope b of the fit in Fig. 13 or from individual pairs $U_{c,max}, h$. For the COSIMA flight model, I_{tot} has been estimated to be $I_{tot} < 1.2 \cdot 10^{-13}\ A$ (Hilchenbach et al., 2017). Additional tests with the COSIMA reference model ("RM") have been carried out in order to validate this value. The setup consisted of an electrically insulated Au metal target and an oscilloscope (capacity target-ground 300 pF and 50 $MOhm$ oscilloscope probe resistance). After an exposure to the primary ion beam of 2 min, the target was discharged via the oscilloscope probe and the total collected charge was derived from the initial discharging voltage. The measured total current, as sum of the primary ion beam and the induced secondary electrons, was in line with the current value referred above. It thus provides an upper limit, since on the Au target the secondary electron yield is higher than on the cometary dust material. The footprint area A_f has been determined experimentally to about 1750 μm^2 . From the slope b of the fit line and the above values, a numerical value for the resistivity of $\rho_r \approx 2.2 \cdot 10^{10}\ \Omega m$ results, which would characterize the cometary material as a bad conductor, but not the best insulator. It is close to that of glass ($\approx 10^{10}$–$10^{12}\ \Omega m$), but less than that of e.g. Polyethylene $(\approx 10^{13}\ \Omega m)$, Teflon $(\approx 10^{14}\ \Omega m)$ or Polystyrene and Sulfur $(\approx 10^{16}\ \Omega m)$, (Chanda, 2018). The asymptotic standard error of the fit line for each of the parameters, U_{off} and slope b, is $\approx 10\%$ and there is a systematic uncertainty of up to $\pm 10\ V$ in the $U_{c,max}$ values and about $\pm 5\ \mu m$ in the h values (in Fig. 13, the corresponding error bars are shown only for one example to simplify the figure). Together with a 10% uncertainty in the beam footprint area A_f, the combined maximum error is estimated to be $\pm 1.0 \cdot 10^{10}\ \Omega m$. Taking into account that the value for I_{tot} forms an upper limit, the conclusion for the specific resistivity as derived from the present data analysis is a lower limit: $\rho_r > 1.2 \cdot 10^{10}\ \Omega m$.

Further information on dust charging comes from the build-up time $\tau = R \cdot C$ of the charge at the agglomerate's elements. Experimental information on τ has been obtained from *in situ* experiments at particle Lou on target 1C3. Spectra have been taken with sampling times of 0.2, 0.75, 2.5, 9.5, 38 and 150 *sec* respectively with about 1 h breaks in between to ensure decharging (Hilchenbach et al., 2017). The finding is that the 2.5 *sec* spectrum already shows a left shoulder with the asymptotic $U_{c,max}$

Table 3
Summary of fit results for 7 particles for the $^{16}O^-$ profile (upper line) and for 3 examples of the $^{32}S^-$ profile (lower line). w_1 is the fraction of ions from uncharged areas. h : dust layer height at SIMS position. The unit of the stretch factor a is $1.956\ ns/\sqrt{M}$, where M is the mass number of the line profile under consideration.

Target- and particle name	ξ	$U_{c,max}$ $[V]$	U_{01} $[eV]$	U_{02} $[eV]$	Δt_p $[nsec]$	w_{el}	w_1	a	h $[\mu m]$
2CF Jessica	1	98	10	4	9.0	0.02	0.23	1601.3	35
1CD Barmal	5	95	10	20	7.0	0.01	0.65	1601.6	35
1D2 Juliette	2	67	10	5	7.5	0.02	0.70	1601.7	18
	2	67	10	10	7.5	0.03	0.35	1601.6	
1D2 Gunter	5	130	10	25	7.0	0.04	0.01	1601.5	57
	5	130	10	20	7.0	0.04	0.00	1601.5	
2D1 Jakub	5	129	10	10	6.0	0.04	0.03	1601.0	55
	5	129	10	10	6.0	0.04	0.01	1601.2	
2D1 David	1	80	10	10	7.0	0.02	0.75	1601.6	20
2D1 Sora	2	100	10	10	6.0	0.02	0.50	1601.6	34

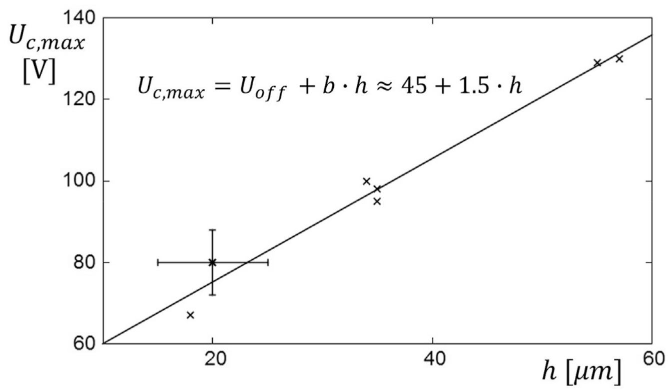

Fig. 13. Maximum charging potential vs. dust layer height.

value at longer sampling times. From this one concludes that the $R \cdot C$ rise time τ has to be less than 1 *sec* (see Fig. 14).

This information, together with the specific resistivity ρ_r , now allows us to derive the real part of relative permittivity ε_r for the elements of the dust agglomerate. For an estimate, assume them to be spherical (with radius $\bar{r}$), having a capacitance $C \approx 4 \cdot \pi \cdot \varepsilon_r \cdot \varepsilon_0 \cdot \bar{r}$ and a resistance $R \approx \rho_r \cdot 2 \cdot \bar{r}/(\pi \cdot \bar{r}^2)$ where ε_0 is the vacuum permittivity. Then the charge-up time becomes size-independent: $\tau \approx 8 \cdot \varepsilon_r \cdot \varepsilon_0 \cdot \rho_r$ and $\varepsilon_r \approx \tau/\ (8 \cdot \varepsilon_0 \cdot \rho_r)$. When considering other shapes than spheres the result does not change much. For instance in the case of a cube (Wintle, 2004) one obtains $\varepsilon_r \approx \tau/(8.3 \cdot \varepsilon_0 \cdot \rho_r)$. From the measured upper limit of τ and the lower limit of ρ_r an upper limit for the relative permittivity follows: $\varepsilon_r\ <\ 1.2$.

A value of ε_r so close to 1 is typical for high porosity materials and one

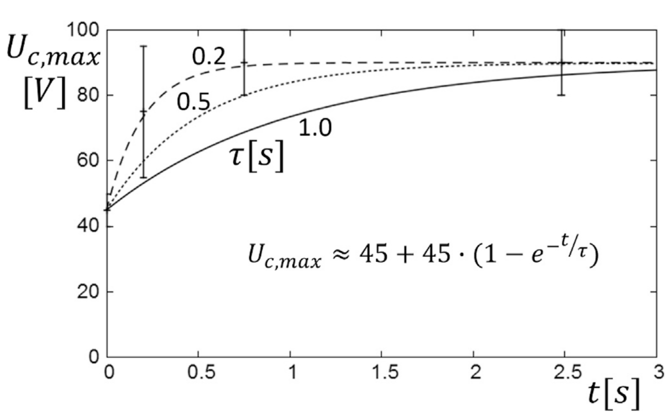

Fig. 14. Dependence of charging potential on spectra sampling time for particle 1C3 Lou.

can use this result to estimate the porosity. This estimate uses data on composition and typical permittivities of the main dust constituents, making use of the effective medium approach for mixtures. Rust et al. (1999) have measured a series of dry volcanic rocks and found the data fitting into an empirical law: $\sqrt{\varepsilon_r} = P + (1 - P) \cdot \sqrt{\varepsilon_{r,c}}$, where $\varepsilon_{r,c}$ is the value of the corresponding compact material and P is the porosity. This power-law with exponent $1/2$ is known as the Birchak equation (Birchak et al., 1974) and has been widely used in optics and refractive index models. In practice, there are several mixing rules based on empirical data and physical principles, such as the well-known Maxwell-Garnett (1904) and Bruggeman (1935) formulae, along with power-law fits with typical exponents $1/2$ and $1/3$ (Maron and Maron, 2008). Yet, all these models predict similar results for high porosity (Sihvola, 2000). For the application of those mixing concepts one needs an estimate of the corresponding compact values. The composition data of the dust collected by COSIMA show that it has a mineral-to-organic ratio of $\approx 0.55/0.45$ by weight (Bardyn et al., 2017). For the electrical properties one needs this ratio by volume, which is $\approx 0.3/0.7$ when assuming a density ratio mineral/organic of ≈ 3 (Greenberg and Li, 1999). The organic part of the investigated particles is found to have high molecular weight (Fray et al., 2016) and typical permittivities for such materials are $\varepsilon_{r,c} \approx 2$ (Chanda, 2018). Mineral values show a greater variety ranging from ≈ 4 (Silica) up to ≈ 8 (Olivine) and ≈ 8.5 (Pyroxene), (e.g. Zheng et al., 2005).

Using the above mineral/organic by-volume ratio, a range of $2.5 < \varepsilon_{r,c} < 3.5$ is estimated for the compact dust mixture following Rust's mixing concept and Fig. 15a shows the corresponding dependence on porosity. One can see that an upper limit of the permittivity $\varepsilon_r = 1.2$ implies a lower limit for the porosity: $P = 0.84$. Allowing for uncertainty in Rust's law, which seems to give a slight overestimate compared to other models, Fig. 15b, we finally estimate for the lower limit of the porosity of the agglomerate's elements a value of 0.8.

6. Discussion and summary

During mass spectrometric analysis we observed dust particle positive charging, reaching maximum values at the center of the primary ion beam's footprint and decreasing radially due to the Gaussian beam profile. In negative ion mode it leads to a characteristic line shape with extended left-shifted contributions ("left shoulder") while in positive ion mode it leads to a very small shift of the line peak of typically few *nsec* and a substantial decrease in transmission since those parts of the exposed area exceeding a charging limit of about 90 V cannot pass the reflectron of the spectrometer. Within the present contribution we focussed on the negative spectra. For a quantitative evaluation of the line asymmetry it is essential to recognize that the left shoulder extensions fully contribute to the total line integral of the spectral mass line under consideration and are not caused by neighbouring mass lines. The fact was already considered in recent COSIMA papers (Fray et al., 2017; Bardyn et al., 2017; Paquette et al., 2017). We could show that, after some initial build-up time, the potential at the dust is determined by a steady DC-like current, approximately following Ohm's law and explicit

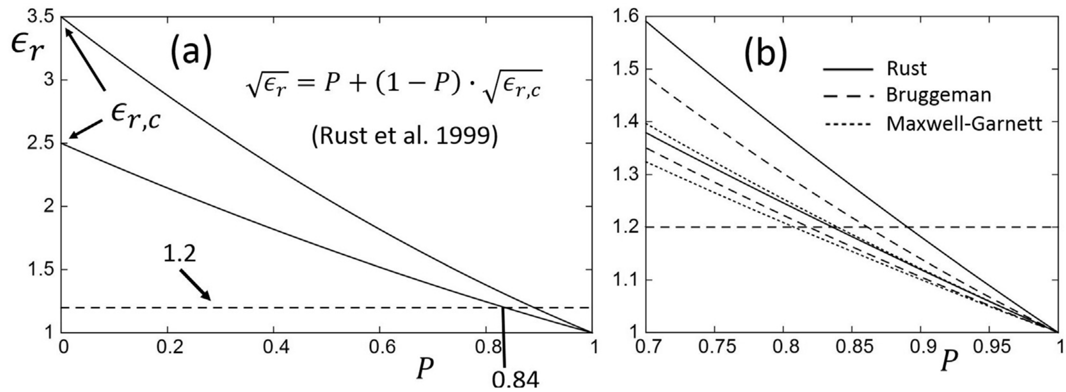

Fig. 15. Real part ε_r of the relative electrical permittivity in dependence on the porosity P. (a): Rust's law, (b) details for high porosity and comparison with other mixing models (Bruggeman and Maxwell-Garnett multiphase).

values for the charging potential could be extracted from the spectra (up to about 130 V for the examples discussed). These charging potentials opened the possibility to derive information on the dust's electrical properties. A lower limit for the electrical resistivity of 67P dust particles could be derived ($\rho_r > 1.2\cdot10^{10}\ \Omega m$). When combining with a measurement of the charge build-up time ($\tau < 1\ s$), an upper bound for the real part of the relative permittivity ε_r could be deduced which turned out to be close to 1 ($\varepsilon_r < 1.2$) and therefore indicating a high porosity of the dust particles ($P > 0.8$). These values refer to the dust's subunits (denoted by „elements“) with sizes approximately between 15 and 40 μm since the footprint of the primary ion beam is limited to an area of about 50 μm diameter such that it contains only few elements (see also Hilchenbach et al., 2017). The CONSERT instrument on Rosetta reported as well the observation of low values for the permittivity ($\varepsilon_r = 1.27 \pm 0.05$) and high porosity ($P = 0.75 - 0.85$) of the cometary interior tracked in the radio frequency region (Kofman et al., 2015; Hérique et al., 2017). The SESAME instrument measurements on the landing near-surface retrieved a maximum permittivity of 3 and a maximum conductivity of $4\cdot10^{-8}(\Omega m)^{-1}$ and explained that with a weathered and sintered surface layer as well as ice content (Lethuillier et al., 2016). For the material collected by COSIMA in the comet's coma, a low permittivity value supports the assumption that the dust particles contained only minimal water or ice after collection and storage within COSIMA for a few days to more than 1 year as the DC relative permittivity of water or ice is much higher than that of minerals or organics (up to values around 100, e.g. Aragones et al., 2010; Pettinelli et al., 2015) and even tiny amounts of them would increase the relative permittivity considerably (Strangway et al., 1972; Anderson, 2008). A high porosity of the collected cometary dust particles is also in line with our findings on the strength, derived from the evaluation of the fragmentation dynamics upon collection (Hornung et al., 2016) as well as on the optical properties, which include high transparency values with a mean free path of the photons of about $20 - 25\ \mu m$ within the dust particle (Langevin et al., 2017).

Acknowledgments

COSIMA was built by a consortium led by the Max-Planck-Institut für Extraterrestrische Physik, Garching, Germany in collaboration with Laboratoire de Physique et Chimie de l'Environnement et de l'Espace, Orléans, France, Institut d'Astrophysique Spatiale, CNRS/Université Paris Sud, Orsay, France, Finnish Meteorological Institute, Helsinki, Finland, Universität Wuppertal, Wuppertal, Germany, von Hoerner und Sulger GmbH, Schwetzingen, Germany, Universität der Bundeswehr München, Neubiberg, Germany, Institut für Physik, Forschungszentrum Seibersdorf, Seibersdorf, Austria, Institut für Weltraumforschung, Österreichische Akademie der Wissenschaften, Graz, Austria and is lead by the Max-Planck-Institut für Sonnensystemforschung, Göttingen, Germany. The support of the national funding agencies of Germany (DLR, grant 50 QP 1801), France (CNES), Austria (FWF, grant P26871-N20), Finland and the ESA Technical Directorate is gratefully acknowledged. We thank the Rosetta Science Ground Segment at ESAC, the Rosetta Mission Operations Centre at ESOC and the Rosetta Project at ESTEC for their outstanding work enabling the science return of the Rosetta Mission.

Supplementary data

Supplementary data to this article can be found online at https://doi.org/10.1016/j.pss.2019.104758.

Appendix. Flight times from spectrometer characteristics

The numerical scheme to model the line shapes uses a simple approach to calculate the flight times. It assumes constant field gradients between the individual grids as well as a flight path along the centerline of the spectrometer (in the following denoted as 1-D approach) and the method is calibrated with fully 3-D SIMION simulations and data from COSIMA's laboratory reference model (RM).

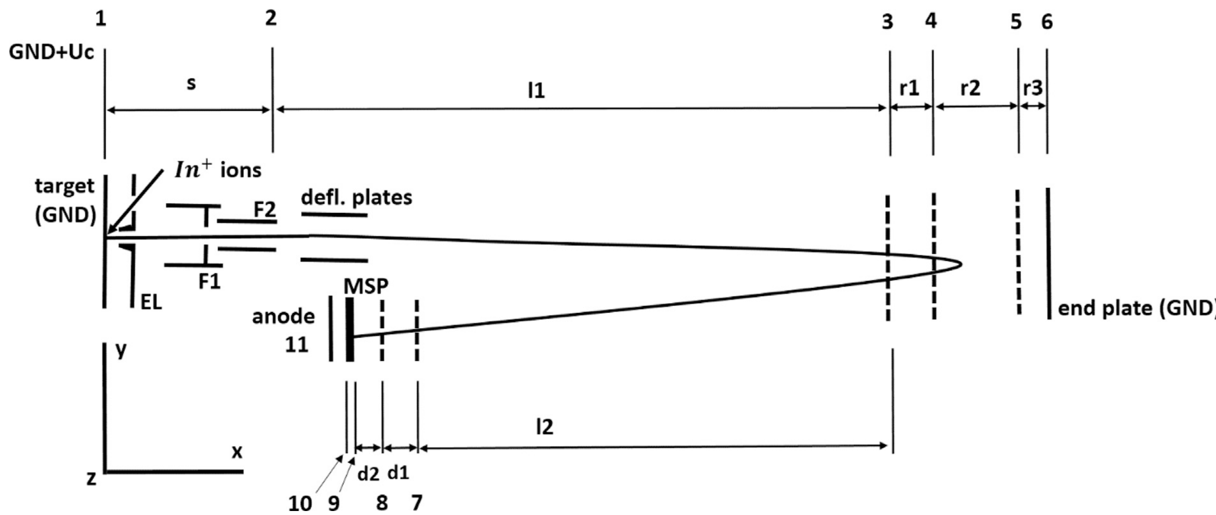

Fig. A.1. Schematic view of the Time-of-Flight section of COSIMA (not to scale).

Fig. A1 shows a schematic overview of the Time-of-Flight setup (Kissel et al., 2007). For better perception it is not to scale, its dimensions are given in Table A1. First is the extraction lens EL at 3 *mm* distance in front of the target, having an opening of diameter 1 *mm*. At the opening's periphery there is a small conical rim, which juts out 1 *mm* from the extraction lens plane. It contributes to collimate the secondary ion beam. Next is a focussing lens F1 at 11 *mm* distance from the target with a 2 *mm* aperture, followed by a concentric cylindrical focussing lens F2 that guides the ions to the first long drift tube section ($2 \rightarrow 3$) with the two extremes at equal voltage U_{DT}, setting a constant velocity and defining the nominal flight kinetic energy of about 1 *keV*. The secondary ion beam can be adjusted by means of 2 pairs of deflection plates (in y- and z-direction). The x-axis is normal to the grids 3 to 6, and z and y define the plane normal to it. The reflectron is of Mamyrin-type (Mamyrin, 2001). In its first segment ($3 \rightarrow 4$), ions are strongly decelerated losing about 80% of their kinetic energy. In its longer second section, the ion's flight direction is reversed between two grids (4,5). After another long drift section at constant velocity ($3 \rightarrow 7$) they pass two entrance grids (7, 8) in front of the microsphere plate detector. The target is at ground level (plus charging if there is any). There are 5 potential settings relevant for the flight-time: U_{EL} for the extraction lens, U_{DT} for the drift tube sections (positions 2, 3 and 7), U_{TOF1} for the entrance grid of the reflectron (position 4), U_{TOF2} at the end of the reflectron (position 5), U_{PA} for the "post acceleration" (position 8). Example values for these 5 potentials are given in Table A2. The potential difference: position 8 minus position 7 is always biased such that secondary electrons released at grid 7 cannot reach the detector. Between grid 8 and the detector inlet (position 9) the potential always increases by 100 *V* (starting from the value of U_{PA} at position 8, see Table A2) such that secondary electrons released at grid 8 makes a small spectral contribution, left-shifted with respect to the ion contribution. The potential difference across the detector microsphere plate ($9 \rightarrow 10$) is always 3000 *V* and the anode is 200 *V* higher than the detector outlet ($10 \rightarrow 11$). However the detector potentials 10 and 11 are only communicated for completeness, they do not enter into the present method for spectra fitting. The detailed electrical field in the lens section ($1 \rightarrow 2$) is determined by the geometrical representation in SIMION (see below) with potential settings of $U_{F1} = U_{DT}/2$ and $U_{F2} = U_{DT}$.

Table A.1
Dimensions of COSIMA's time-of-flight section in *mm*.

s	l_1	r_1	r_2	r_3	l_2	d_1	d_2
18.26	536.0	20.0 – 0.3	40.0 + 0.3	10.0	509.7	6.94	2.85

Table A.2
Example values for the 5 potential settings (in *Volts*) for the flight model ("XM") and the laboratory reference model ("RM") of COSIMA, each for negative and positive ion modes (corresponding to the examples of Figs. 8 and 4 respectively).

	XM neg.	XM pos.	RM neg.	RM pos.	Positions (Fig. A1)
U_{EL}	+2997	−2998	+2991	−3000	"EL"
U_{DT}	+1000	−1000	+997	−1000	2,3,7
U_{TOF1}	+200.6	−200.1	+205.7	−205.1	4
U_{TOF2}	−90.9	+98.3	−87.8	+88.1	5
U_{PA}	+859	−2998	+908	−3066	8

Calibration of the simple quasi 1-D approach uses fully 3-dimensional numerical simulations with the SIMION® software (Dahl, 1997) together with COSIMA's geometry data (Kissel et al., 2007). The simulations showed that the potential gradients between the grids are not exactly linear and also they do not change abruptly at the grid locations but in a smooth way. On the other hand, the line shifts depend in an extremely sensitive way on the electrical fields in the reflectron. It turned out that a correction for these effects is possible by a very minor tuning of two lengths by 0.3 *mm* (see Table A1) leading to a precise agreement between 1-D and SIMION. Fig. A2 shows the resulting time shifts. They depend on the initial kinetic energy e_k of the ions at emission from the target (see Zubarev, 1996). Experimental shifts of the line maximum obtained with the COSIMA laboratory reference model RM (see Fig. 4) are well reproduced. The present paper focusses on negative spectra, but the above 1-D approach applies similarly to the case of positive ions. The lower part of Fig. A2 (negative U_c values) is identical to the case of positive charging in positive mode, since negative charging in negative ion mode is equivalent to a positive charging in positive ion mode. As can be seen in the figure, the corresponding time shifts are very small (a few TOF units, depending on the ion mass number, for the highest possible charge values of ≈ 90 *V* limited by the transmission in positive mode, see below).

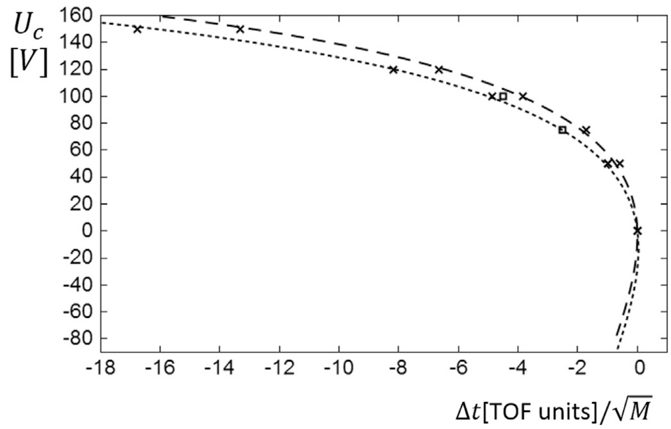

Fig. A.2. Time shift Δt due to charging for the COSIMA laboratory model RM, negative ion case, for various values of the particle surface potential U_c. Dotted line: initial kinetic energy $e_k = 0\ eV$, dashed line: $e_k = 10\ eV$, together with SIMION values (crosses) and RM oxygen data (squares). 1 TOF time bin unit is 1.956 *nsec*. *M* is the ion mass number.

The SIMION simulations revealed that charging not only leads to a time-shift but also to a reduction of transmission, roughly a factor of 2 at $U_c = 100\ V$ for negative spectra, that results in a small, but significant modulation of the line shape. In the simulations, we considered Maxwellian distribution for the emission velocities with U_0 varying between 5 and 30 eV and with $cos^2\theta$ and $\cos\theta$ angular distributions, where $\theta = 0$ denotes the target normal. It turned out that the transmission reduction is practically independent of U_0 in this range and almost identical for both angular distributions, following the reduction factor function $f_{tr} = 1 - 0.0053 \cdot U_c + 8.5 \cdot 10^{-6} \cdot U_c^2$, that has been used in the model of Sec. 3. It holds up to $U_c \approx 175\ V$ which includes the range of charging potentials found in the examples of the present report. For positive ions, the transmission dependence on U_c reaches a cutoff at much lower charging potentials at $U_c \approx U_{TOF2}$ ($\approx 90\ V$) when the ions hit the backplate of the reflectron (position 6). Theoretically, transmission does not depend on the ion mass. The effect of charging, in the case of negative ions, is thus a marked line shift and a continuous decrease in transmission for charging potentials up to about 200 V and for positive ions a very small line shift and a sharp cutoff of transmission at about 90 V.

References

Anderson, O., 2008. Dielectric relaxation of the amorphous ices. J. Phys. Condens. Mater. 20, 244115. https://doi.org/10.1088/0953-8984/20/24/244115.

Aragones, J.L., et al., 2010. Dielectric constant of ices and water: a lesson about water interactions. J. Phys. Chem. A 11523, 5745–5758, 2011. https://doi.org/10.1021/jp105975c.

Bardyn, A., et al., 2017. Carbon-rich dust in comet 67P/Churyumov-Gerasimenko measured by COSIMA/Rosetta. Mon. Not. R. Astron. Soc. 469, S712–S722. https://doi.org/10.1093/mnras/stx2640.

Bentley, M.S., et al., 2016. Aggregate dust particles at comet 67P/Churyumov–Gerasimenko. Nature 537, 73–75. https://doi.org/10.1038/nature19091.

Birchak, J.R., et al., 1974. High dielectric constant microwave probes for sensing soil moisture. Proc. IEEE 62 (1), 93–98. https://doi.org/10.1109/proc.1974.9388.

Boivin, A.L., et al., 2018. Broadband measurements of the complex permittivity of carbonaceous asteroid regolith analog materials. J. Geophys. Res.: Planets 123. https://doi.org/10.1029/2018JE005662.

Bruggeman, D.A.G., 1935. Berechnung verschiedener physikalischer Konstanten von heterogenen Substanzen. 1. Dielektrizitätskonstanten und Leitfähigkeiten der Mischkörper aus isotropen Substanzen. 5. Folge. Band 24, 636–664. https://doi.org/10.1002/andp.19354160705.

Campbell, M.J., Ulrichs, J.R., 1969. Electrical properties of rocks and their significance for lunar radar observations. J. Geophys. Res. 74 (25), 5867–5881. https://doi.org/10.1029/JB074i025p05867.

Chanda, M., 2018. CRC Handbook of Plastics Technology, fifth ed., vol. 13. CRC Press, ISBN 978-1-4987-8621-8, pp. 369–371. https://doi.org/10.1201/9781315155876.

Dahl, D.A., 1997. INEEL, Idaho Falls, Idaho 83415, the SIMION Software Manual, 1997 (And Later Versions).

Fray, N., et al., 2016. High-molecular-weight organic matter in the particles of comet 67P/Churyumov-Gerasimenko. Nature 538, 72–74, 06 October 2016. https://doi.org/10.1038/nature19320.

Fray, N., et al., 2017. Nitrogen to carbon atomic ratio measured by COSIMA in the particles of comet 67P/Churyumov-Gerasimenko. Mon. Not. R. Astron. Soc. https://doi.org/10.1093/mnras/stx2002.

Greenberg, J.M., Li, A., 1999. Morphological structure and chemical composition of cometary nuclei and dust. Space Sci. Rev. 90, 149–161. https://doi.org/10.1023/a:1005298014670.

Hérique, A., et al., 2017. Cosmochemical implications of CONSERT permittivity characterization of 67P/CG. Mon. Not. R. Astron. Soc. 462 (1), S516–S532, 16 November 2016. https://doi.org/10.1093/mnras/stx040.

Hickson, D., et al., 2018. Near surface bulk density estimates of NEAs from radar observations and permittivity measurements of powdered geologic material. Icarus 306, 16–24. https://doi.org/10.1016/j.icarus.2018.01.018.

Hilchenbach, M., et al., 2016. Comet 67P/Churyumov–Gerasimenko: close-up on dust particle fragments. Astrophys. J. Lett. 816, L32. https://doi.org/10.3847/2041-8205/816/2/L32.

Hilchenbach, M., et al., 2017. Mechanical and electrostatic experiments with dust particles collected in the inner coma of comet 67P by COSIMA onboard Rosetta. Phil. Trans. R. Soc. A375, 20160255. https://doi.org/10.1098/rsta.2016.0255.

Hornung, K., et al., 2016. A first assessment of the strength of cometary particles collected in-situ by the COSIMA instrument onboard ROSETTA. Planet. Space Sci. 133, 63–75. https://doi.org/10.1016/j.pss.2016.07.003.

Hornung, K., et al., 2014. Collecting cometary dust particles on metal blacks with the COSIMA instrument onboard ROSETTA. Planet. Space Sci. 103, 309–317. https://doi.org/10.1016/j.pss.2014.08.011.

Isnard, R., et al., 2019. H/C elemental ratio of the refractory organic matter in cometary particles of 67P/Churyumov-Gerasimenko. A&A 630 (A27). https://doi.org/10.1051/0004-6361/201834797.

Kissel, J., the COSIMA team, 2007. COSIMA: high resolution time-of-flight secondary ion mass spectrometer for the analysis of cometary dust particles onboard ROSETTA. In: Schulz, R., Alexander, C., Boenhardt, H., Glassmeier, K.H. (Eds.), ESA's Mission to the Origin of the Solar System. Springer, NewYork, pp. 201–242. https://link.springer.com/article/10.1007/s11214-006-9083-0.

Kofman, W., et al., 2015. Properties of the 67P/Churyumov-Gerasimenko interior revealed by CONSERT radar. Science 349 (6247). https://doi.org/10.1126/science.aab0639, 31 July 2015.

Langevin, Y., et al., 2016. Typology of dust particles collected by the COSIMA mass spectrometer in the inner coma of 67P/Churyumov Gerasimenko. Icarus 271, 76–97. https://doi.org/10.1016/j.icarus.2016.01.027.

Langevin, Y., et al., 2017. Optical properties of cometary particles collected by the COSIMA mass spectrometer on-board Rosetta during the rendezvous phase around comet 67P/Churyumov–Gerasimenko. MNRAS 469, S535–S549. https://doi.org/10.1093/mnras/stx2070.

Lethuillier, A., et al., 2016. Electrical properties and porosity of the first meter of the nucleus of 67P/Churyumov-Gerasimenko, as constrained by the Permittivity Probe SESAME-PP/Philae/Rosetta. A&A 591, A32. https://doi.org/10.1051/0004-6361/201628304, 2016.

Mamyrin, B.A., 2001. Time-of-flight mass spectrometry (concepts, achievements, and prospects). Int. J. Mass Spectrom. 206, 251–266. https://doi.org/10.1016/s1387-3806(00)00392-4.

Mannel, T., et al., 2016. Fractal cometary dust – a window into the early Solar system. Mon. Not. R. Astron. Soc. 462, S304–S311. https://doi.org/10.1093/mnras/stw2898.

Maron, N., Maron, O., 2008. Criteria for mixing rules application for inhomogeneous astrophysical grains. Mon. Not. R. Astron. Soc. 391 (2), 738–764. https://doi.org/10.1111/j.1365-2966.2008.13908.x.

Maxwell Garnett, J.C., 1904. Colours in metal glasses and in metallic films. Philos. Trans. R. Soc. London, Ser. A 203, 385–420. https://doi.org/10.1098/rsta.1904.0024.

Merouane, S., et al., 2016. Dust particle flux and size distribution in the coma of 67P/Churyumov-Gerasimenko measured in situ by the COSIMA instrument on board Rosetta. Astron. Astrophys. 596, A87. https://doi.org/10.1051/0004-6361/201527958.

Merouane, S., et al., 2017. Evolution of the physical properties of dust and cometary dust activity from 67P/Churyumov–Gerasimenko measured *in situ* by *Rosetta*/COSIMA. Mon. Not. R. Astron. Soc. 469, S459–S474. https://doi.org/10.1093/mnras/stx2018.

Paquette, J.A., et al., 2016. Searching for calcium-aluminum-rich inclusions in cometary particles with Rosetta/COSIMA. Meteorit. Planet. Sci. 51 (Nr 7), 1340–1352. https://doi.org/10.1111/maps.13043 erratum: Vol. 53, Nr 3, 549–550 (2018). https://doi.org/10.1111/maps.12669.

Paquette, J.A., et al., 2017. The $^{34}S/^{32}S$ isotopic ratio measured in the dust of comet 67P/Churyumov–Gerasimenko by Rosetta/*COSIMA*. Mon. Not. R. Astron. Soc. 469 (Suppl. l_2, 21), S230–S237. July 2017. https://doi.org/10.1093/mnras/stx1623.

Paquette, J.A., et al., 2018. The oxygen isotopic composition ($^{18}O/^{16}O$) in the dust of comet 67P/Churyumov-Gerasimenko measured by COSIMA on-board Rosetta. Mon. Not. R. Astron. Soc. 477 (3), 3836–3844. https://doi.org/10.1093/mnras/sty560. July 2018.

Pettinelli, E., et al., 2015. Dielectric properties of Jovian satellite ice analogs for subsurface radar exploration: a review. Rev. Geophys. 53, 593–641. https://doi.org/10.1002/2014RG000463.

Rotundi, A., et al., 2015. Dust measurements in the coma of comet 67P/Churyumov–Gerasimanko inbound to the Sun. Science 347 (6220). https://doi.org/10.1126/science.aaa3905.

Rust, A.C., et al., 1999. Dielectric constant as a predictor of porosity in dry volcanic rocks. J. Volcanol. Geotherm. Res. 91, 79–96. https://doi.org/10.1016/s0377-0273(99)00055-4.

Schulz, R., et al., 2015. Comet 67P/Churyumov-Gerasimenko sheds dust coat accumulated over the past four years. Nature 518, 216–218. https://doi.org/10.1038/nature14159.

Sihvola, A., 2000. Mixing rules with complex dielectric coefficients. Subsurf. Sens. Technol. Appl. 1 (4) https://doi.org/10.1023/A:1026511515005.

Strangway, D.W., et al., 1972. Electrical properties of lunar soil dependence on frequency, temperature and moisture. Earth Planet. Sci. Lett. 16, 275–281. https://doi.org/10.1016/0012-821x(72)90203-8.

Werner, H.W., Morgan, A.E., 1976. Charging of insulators by ion bombardment and its minimization for secondary ion mass spectrometry (SIMS) measurements. J. Appl. Phys. 47, 1232. https://doi.org/10.1063/1.322845.

Wintle, H.J., 2004. The capacitance of the cube and square plate by random walk methods. J. Electrost. 62, 51–62. https://doi.org/10.1016/j.elstat.2004.04.005.

Zheng, Y., et al., 2005. Measurement of the complex permittivity of dry rocks and minerals: application of polythene dilution method and Lichtenecker's mixing formulae. Geophys. J. Int. 163, 1195–1202. https://doi.org/10.1111/j.1365-246X.2005.02718.x.

Zubarev, R.A., et al., 1996. Kinetic energies of secondary ions in MeV and keV particle-induced desorption. Rapid Commun. Mass Spectrom. 10, 1966–1974. https://doi.org/10.1002/(sici)1097-0231(199612)10:15<1966::aid-rcm783>3.0.co;2–3.